

Supporting Information for:

Activationless Charge Transport across 4.5 to 22 nm in Molecular Electronic Junctions

Haijun Yan^a, Adam Johan Bergren^a, Richard L. McCreery^{a,b} *

Maria Luisa Della Rocca^c, Pascal Martin^d, Philippe Lafarge^c, Jean Christophe Lacroix^d

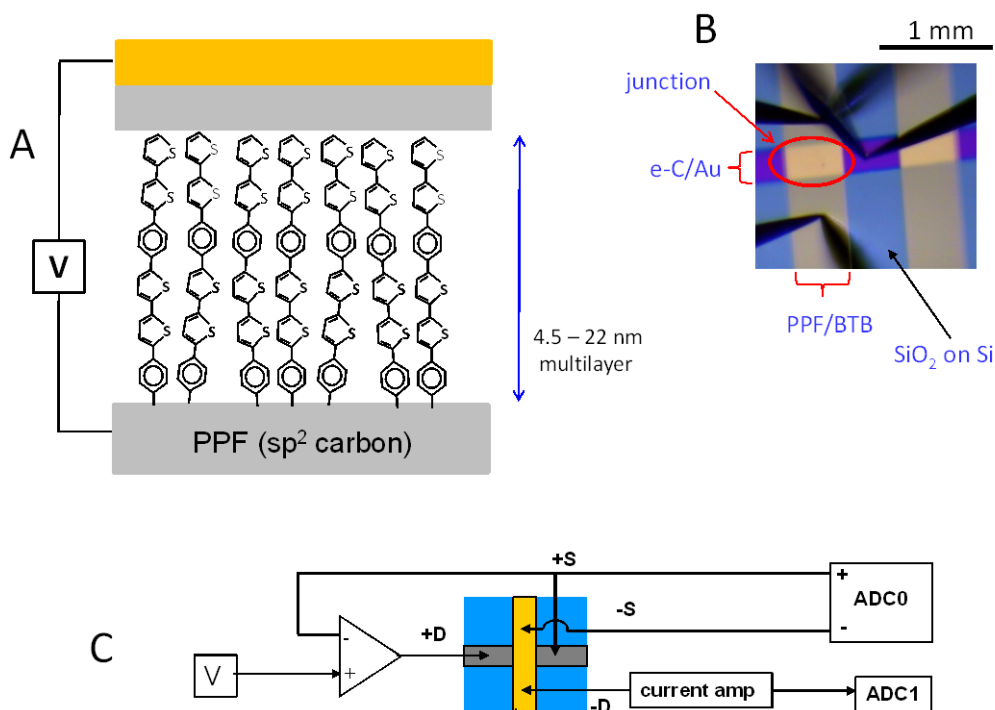
a. National Institute for Nanotechnology, Edmonton, AB, Canada T6G 2M9; b. Department of Chemistry, University of Alberta, Edmonton, AB, Canada T6G 2G2; c. Laboratoire Matériaux et Phénomènes Quantiques (MPQ), Unité Mixte de Recherche 7162, Centre National de la Recherche Scientifique (CNRS), Université Paris Diderot, Sorbonne Paris Cité, 75205 Paris Cedex 13, France; d. Laboratoire Interfaces, Traitements, Organisation et Dynamique des Systèmes (ITODYS), Unité Mixte de Recherche 7086, Centre National de la Recherche Scientifique (CNRS), Université Paris Diderot, Sorbonne Paris Cité, 75205 Paris Cedex 13, France

Contents:

1. Experimental Schematics
2. Junction fabrication
3. Measurement of Molecular Layer Thickness and Microscopy
4. Representative Current-Voltage results
5. Plots of $\ln J$ vs $\ln V$
6. Attenuation coefficients (β) for various conditions
7. Supplemental JV curves for $T = 6-300$ K range
8. Variable Range Hopping plots
9. Activation barrier dependence on electric field

1. Experimental schematics

Figure S1A shows a schematic cross section of the all-carbon molecular junction, consisting of oligomers of bis-thienyl-benzene (BTB) between a carbon substrate and a carbon top contact. The molecular layer is partially ordered with covalent bonding to the PPF substrate, and has a range of thickness from 4.5 to 22 nm. Figure S1B shows an image of the top of two completed junctions, which occur at the intersection of orthogonal lines of PPF and top contact, along with three of the four probes used to make electrical contact. Figure S1C is a schematic of the 4-wire circuit used for current/voltage measurements, which compensates for lead and probe contact resistances. Junction area was 0.00125 cm^2 in all cases.



Figure

S1A. Junction schematic (A), image of completed junction from above, showing three of the four contact probes (B), and electronic schematic of 4-wire system used for JV measurements (C). ADC0 and ADC1 are inputs to a National Instruments 6111 data acquisition board, and the “current amp” is a Stanford Research Systems 570 current amplifier. Applied voltage (V) is provided by DAC0 from the 6111 board, and was scanned at 1000 V/sec in most cases. For currents < 200 nA which occurred at low bias a Keithley 6517B electrometer in two electrode configuration was used to measure a series of discrete bias values.

I-V curves were measured by different methods depending on the thickness of the molecular layer. Thus, for thin layers where capacitive current is small, voltage scans were used, typically at 100 or 1000 V/s. As the thickness and capacitive current increased, the DC characteristic was obtained by either slowing the scan rate to as low as 0.5 V/s, or by a series of DC voltage pulses. In the latter case, voltage pulses were applied every 0.1 V or so, and the capacitive current was allowed to decay prior to taking a current reading.

2. Junction Fabrication

The “crossed junction” design has been reported in a series of papers (1-10), and was used here with bis-thienyl benzene (BTB) as the molecular component, a substrate of pyrolyzed photoresist film (PPF) (11) and a top contact of electron-beam deposited carbon (e-C) and Au. Preparation of PPF has been described in detail previously (1, 11), but consists of photolithographic patterning of four parallel 0.5 mm wide lines of photoresist on Si/SiO₂ surfaces followed by pyrolysis in a flowing H₂/N₂ atmosphere at 1100 °C. The result is four conducting, sp² hybridized carbon “stripes” with surface roughness < 0.4 nm rms.

The precursor to the BTB diazonium reagent, 1-(bithien-2-yl)-4-aminobenzene [BTAB] was prepared as described previously (4), then its diazonium ion was prepared in-situ before electrochemical modification of PPF as follows: An acetonitrile (ACN) solution (20 mL) containing BTAB (5mM, ~2.6mg) and tetrabutylammonium tetrafluoroborate (TBABF₄, 0.1M, ~0.66g) as supporting electrolyte was prepared and degassed with high purity argon for ~30 minutes. Tert-butyl nitrite (36μL) was then added to the above solution and was stirred for 15 min before electrografting was started. Electrografting was carried out with cyclic voltammetry in the above solution using PPF as working electrode, Ag/Ag⁺ as reference electrode and Pt as counter electrode. Cyclic voltammetric sweeps were initiated from +400 mV to selected negative potentials at 100 mV/s. Various thicknesses were obtained by varying the negative potential range and number of scans, as noted in table S1. After surface modification, samples were thoroughly rinsed with copious ACN and dried with Ar. Typical values for the surface roughness (rms) determined with tapping-mode AFM were 0.4 nm for bare PPF and 0.5 nm for a 10.5nm BTB film on PPF. After electrografting, orthogonal lines (250 μm wide) of 10 nm e-C and 15 nm Au were applied to the PPF/BTB “stripes” through a shadow mask by electron-beam deposition, as described previously (7). Raman spectroscopy of similar PPF/molecule/e-C/Au junctions through both the top contact and a transparent substrate before and after e-C/Au deposition revealed no observable structural changes to the molecular layer during top contact deposition (5, 7, 12).

3. Measurement of Molecular Layer Thickness and Microscopy

Oligo-BTB film thicknesses on PPF were determined by an Atomic Force Microscopy (AFM) “scratching” technique described previously (6, 13). Thickness measurements were carried out on PPF/BTB immediately adjacent to one of the junctions of each sample. First, contact mode was applied to scratch a trench (1 x 1 μm) in the molecular layer, with the result shown in figure S2A. A set point (0.25V) was used to remove the molecules but not damage the underlying PPF substrate. A 5 x 5 μm tapping-mode image was then obtained in the area surrounding and including the trench. Finally, the image was analyzed within the area defined by the white rectangle in Figure S2A to determine the difference in height between the bottom of the trench and the upper surface of the molecular layer. A histogram generated from the height data was fit by two separate Gaussian functions (for the two different height distributions), with the height determined as the difference between the centers of the two functions and the uncertainty

given as the quadrature addition of the two best-fit σ values. Table S1 lists all molecular layer thicknesses determined in the same way. To reflect the uncertainty in thickness, the values given in the main paper are rounded to the nearest 0.5 nm.

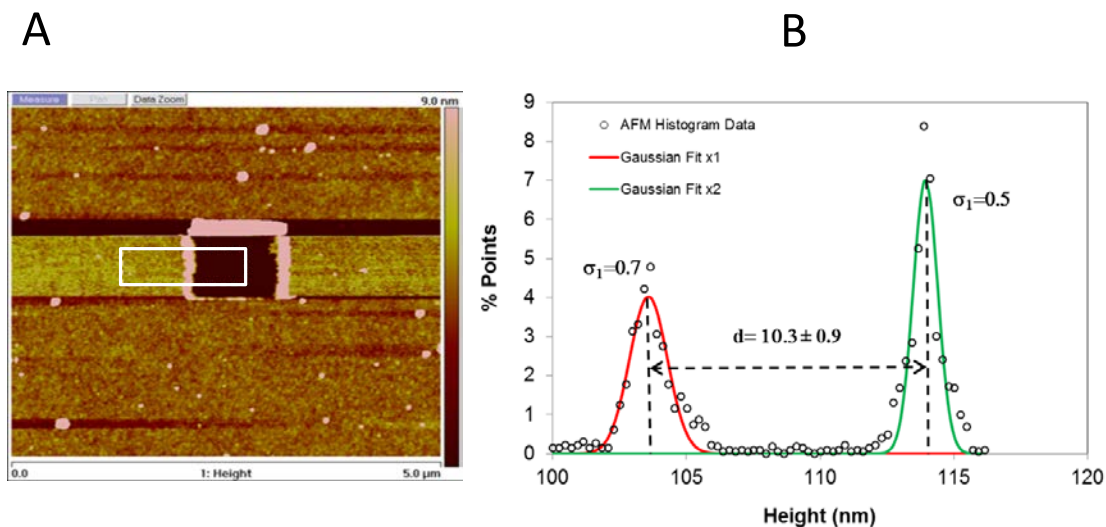


Figure S2. (A) 5 x 5 μm tapping mode image of a 1 x 1 μm “trench” made in a PPF/BTB layer using contact mode AFM. (B): histogram of heights determined within the white rectangle of the AFM image. Uncertainty in thickness is the quadrature addition of the two Gaussian σ values.

Table S1: BTB film derivatization conditions and corresponding film thicknesses (in nm) determined as shown in figure S2:

Derivatization Conditions	AFM Thickness
+0.4V to -0.4V, 1 scan	4.5 \pm 0.7
+0.4V to -0.6V, 1 scan	5.2 \pm 0.9
+0.4V to -0.4V, 2 scans	6.9 \pm 0.6
+0.4V to -0.6V, 2 scans	8.1 \pm 0.7
+0.4V to -0.4V, 4 scans	10.4 \pm 0.8
+0.4V to -0.6V, 4 scans	12.8 \pm 0.9
+0.4V to -0.6V, 6 scans	16 \pm 1
+0.4V to -0.6V, 10 scans	22 \pm 1

Layer thickness and integrity were confirmed by obtaining a STEM image of a completed PPF/BTB(10 nm)/e-C(10 nm)/Au(20 nm) junction sectioned by a focused ion beam. The image of figure S3 was obtained with a Hitachi S5500 STEM by Peng Li of the NINT microscopy facility. From top to bottom in the image are the PPF, BTB, e-C,

and Au layers of the junction plus an addition e-C layer added to protect the sample during ion beam sectioning.

FIB/TEM of PPF/bisthiophenylbenzene/e-Carbon/Au:

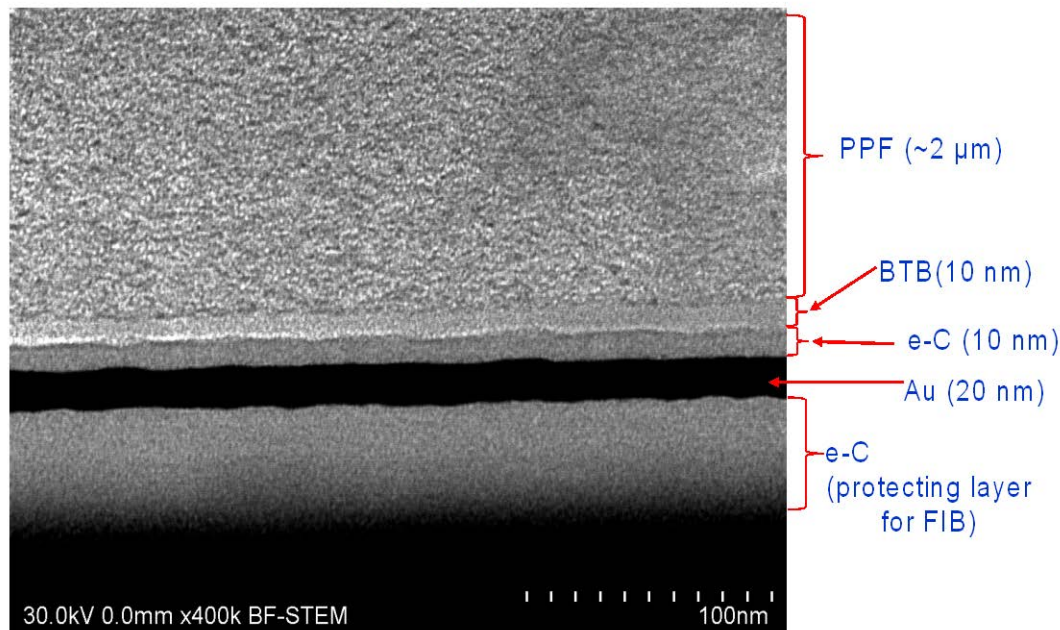


Figure S3. A STEM image of PPF/BTB(10 nm)/e-C(10 nm)/Au(20 nm) junction obtained after sectioning with a focused ion beam (FIB). e-Carbon layer at bottom was applied preceding FIB sectioning to protect the junction layers.

4. Representative Current-Voltage results

As reported previously, relative standard deviations (*rsd*) for the current density measured for a series of independent molecular junctions made with the procedures outlined above are in the range of 10-20% (6, 7). An example for PPF/BTB/e-C/Au junctions is shown in figure S4A, which is an overlay of *JV* curves for seven different junctions with a BTB thickness of 22 nm. The *rsd* of *J* for the seven junctions varies from 8.3% at $V=1$ V to 19% at 0.5 V, with an average for this voltage range of 11.1%. The average for the -0.5 to -1.0 V range was 11.5% with a maximum of 15% at $V = -1$ V. Figure S4B is an expansion of the low voltage range for 13, 16, and 22 nm BTB junctions at 300K, showing the overlap of the 16 and 22 nm curves in the ± 0.4 V range. The attenuation coefficient β for the 16-22 nm curves is $(0.015 \pm 0.005) \text{ nm}^{-1}$ at $V = 0.3$ V, 0.037 ± 0.007 at $V = 0.5$ V, and $0.133 \pm .003$ at $V = 1.0$ V (see table S3). Stated errors are standard deviations of ten points determined for bias values centered on the stated voltage.

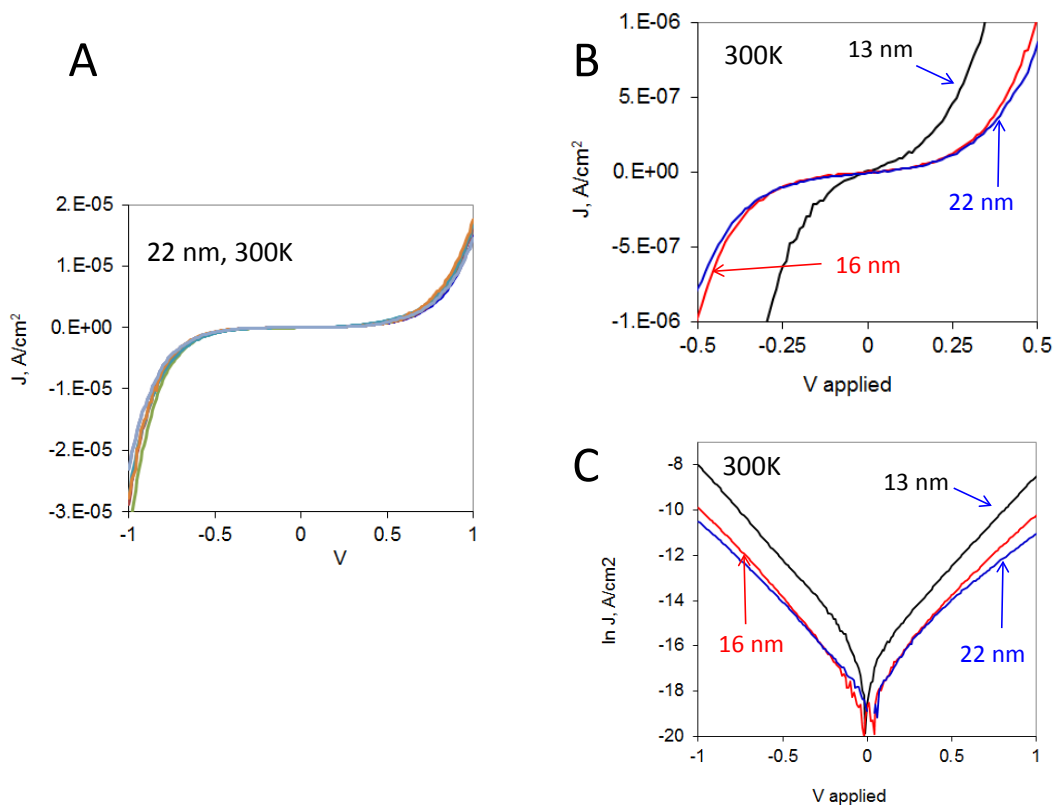


Figure S4. (A) Overlay of seven JV curves for independent PPF/BTB(22 nm)/e-C(10 nm)/Au(20 nm) junctions obtained at 300K (see supplemental text for statistics). (B) Magnified low bias region for 13, 16, and 22 nm BTB junctions at 300K, determined under identical conditions. (C) Same data as B, plotted with $\ln J$ axis.

5. Plots of $\ln J$ vs $\ln V$

Plots of $\ln J$ vs $\ln V$ are useful for indicating mechanism, and several are shown in figure S5 for various BTB thicknesses and temperatures. A listing of the slopes of all cases examined is shown in Table S2 for both low and high bias ranges. The intercept of $d(\ln J)/d(\ln V)$ at low V is 1.11 ± 0.14 for the 5-22 nm thickness range at 300 K, indicating ohmic behavior at low bias. This slope increases to 12-15 for $d= 8.0, 10.5,$ and 22 nm as the bias is increased to ~ 5 V, indicating a major departure from ohmic behavior.

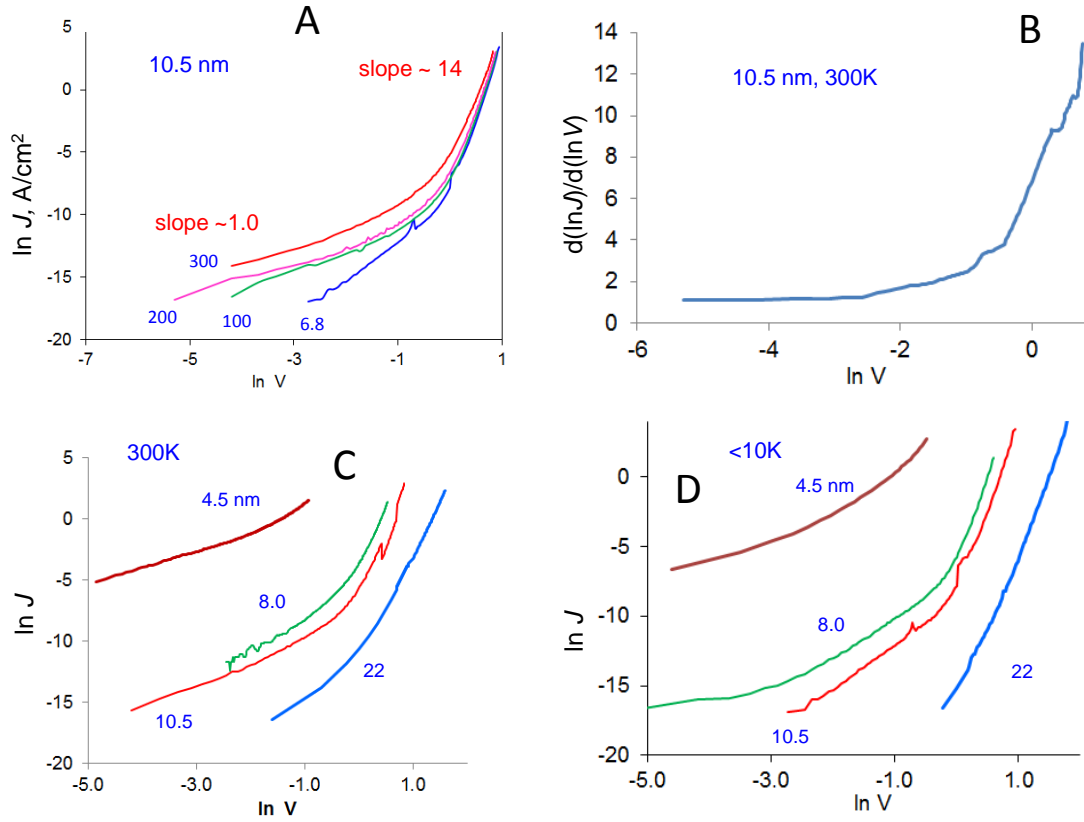


Figure S5. $\ln J$ vs $\ln V$ for several temperatures and BTB thicknesses. (A) 10.5 BTB thickness at indicated temperatures from 6.8 to 300 K. Approximate slopes are indicated, and a full listing is in Table S2. (B) slope of $\ln J$ vs. $\ln V$ plot vs $\ln V$ for 10.5 nm BTB at 300K; (C) Plots for four thicknesses at 300 K; (D) Plots for four thicknesses at <10 K.

Table S2: Slopes and intercepts of $\ln J$ vs $\ln V$ plots

	thickness	V range	slope @ 300K	slope, <10K	d, nm	intercept*
Low V:	4.5 nm	0.01-0.11	2.17	1.44	5.0	1.03
	8.0	0.01 - 0.10	1.92	0.91	7.0	0.96
	10.5	0.01-0.10	1.15	2.47	8.0	1.23
	22	0.8 - 1.3	3.97	7.71	10.5	1.03
				13	1.31	
Hi V:	4.5	0.5-0.6	1.50	1.52	16	1.22
	8.0	1.7-1.8	13.20	13.80	22	0.97
	10.5	1.9-2.5	14.06	14.05	mean	1.11
	22	4.9-5.2	12.08	15.06	st. dev	0.14

* intercept of $d(\ln J)/d(\ln V)$ at $V=0$ and 300 K

6. Attenuation coefficients (β) for various conditions

Table S3 lists β values with units of nm^{-1} derived from JV curves at various temperatures and bias ranges for the 8 thicknesses listed in table S1. Slopes of $\ln J$ vs d plots, many of which are shown in figure 2 of the main text, determined from least squares fits to 2-4 BTB thicknesses are listed. Values for high bias and thin BTB layers could not be determined because the current exceeded the instrumental limit (5 mA). Figure S4 shows that the 16 nm and 22 nm JV curves are indistinguishable in the range of ± 0.4 V, with the result being a small β for the 12-22 nm range (0.015 at $V = 0.3$ V and 0.04 at $V = 0.5$ V)

Table S3. Attenuation coefficient β (nm^{-1}) for various V and T

thickness range:	4-8 nm		8-16 nm		16-22 nm	
V @ 300K	β^*	σ	β^*	σ	β^*	σ
0.3 V	2.86	0.32	0.81	0.17	0.015	0.005
0.5	2.4	0.44	0.79	0.17	0.037	0.007
1.0	2.89	0.32	0.88	0.17	0.13	0.003
1.5			0.95	0.17	0.15	
2.0			1.05		0.18	
3.0			0.75		0.28	
V @ 200K						
0.8	3.04		1			
1.5			0.9			
2.0			1.06			
V @ 100K						
0.8	3.06		1.12			
1.5			1.04			
2.0			1.18			
V @ 50K						
0.8	3.17		1			
1.5			1.14			
2.0			1.45			
V @ 6-8K						
0.5	3.02		0.65			
0.8	3.28		0.86			
1.5			1.03			
2.0			1.33			
mean	2.97		1.00		0.13	
st. dev.	0.266		0.197		0.097	
N	8		19		6	

* for 4.5-8 nm, β is the least-squares slope of 3-5 points of the plot of $\ln J$ vs junction thickness, and has units of nm^{-1} . σ is the standard deviation of the least squares slope. For 16-22 nm, β and σ were determined from 10 bias points surrounding the indicated bias.

7. Supplemental JV curves for $T = 6-300$ K range

Figure S6 shows JV curves at the indicated temperatures for 4.5 and 8.0 nm BTB junctions, obtained with the same conditions as Figures 3A and 3B of the main text. The T dependence for the 4.5 nm device is likely due to Fermi function broadening in the contacts, as proposed elsewhere (2, 14). Scans were independent of scan rate in the range 10-1000 V/s (excluding capacitive current when observed, see section 1), and could be repeated many times. In no case were effects of memory or fatigue observed, such as hysteresis or slow changes with repetitive scanning.

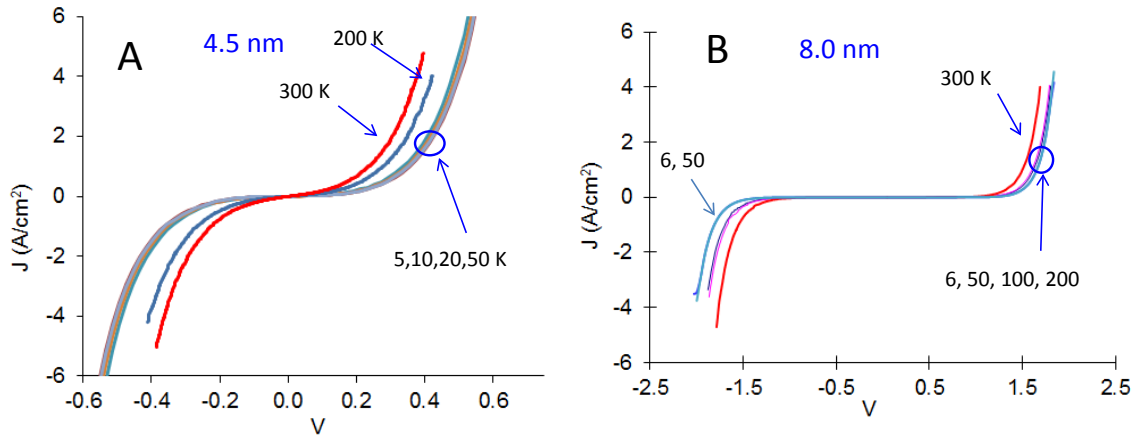


Figure S6. JV curves for 4.5 nm (A) and 8.0 nm (B) BTB junctions obtained at the indicated temperatures. Identical conditions as those for Figures 3A and 3B of the main text.

8. Variable Range Hopping (VRH) plots

The contribution of VRH to transport in disordered solids is characterized by linear plots of $\ln J$ vs $T^{-1/2}$ for one-dimensional Mott VRH or Efros-Shklovskii VRH, or linear $\ln J$ vs $T^{-1/4}$ for 3-dimensional Mott VRH. Such plots are shown for the 200-300 K range and three BTB thicknesses in figures S7A and S7B, along with a theoretical line calculated from standard VRH equations (15). Linearity was not observed for any of the experimental results in the conditions studied, and agreement between observations and VRH prediction was not observed for any physically reasonable parameters.

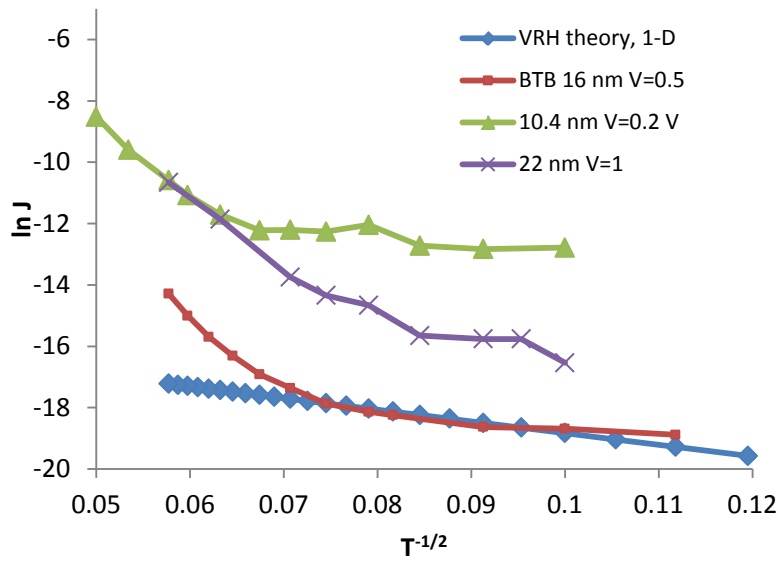


Figure 7A. Comparison of 1-dimensional Mott VRH theory with experimental observations. Theoretical line calculated for a prefactor of 3×10^{-7} A/cm², localization length of 16 nm and density of states of 2×10^7 eV⁻¹ cm⁻¹

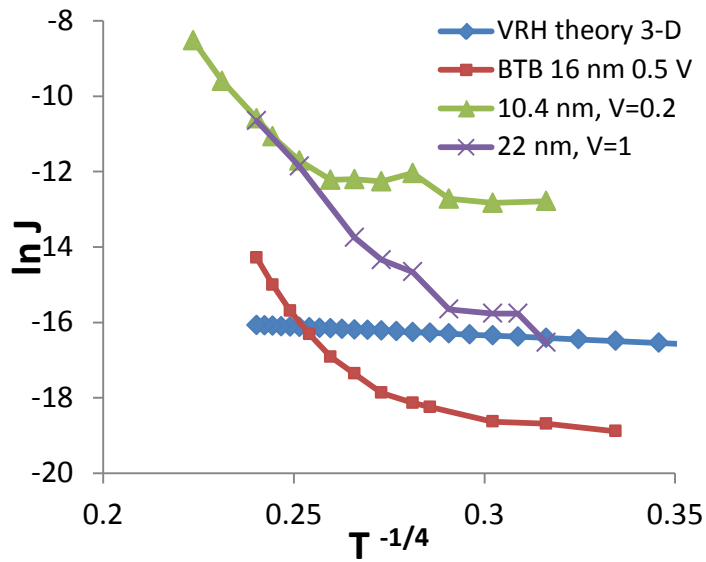


Figure S7B . Comparison of 3-dimensional Mott VRH theory with experimental observations. Theoretical line calculated for a prefactor of 3×10^{-7} A/cm², localization length of 16 nm and density of states of 1.6×10^{20} eV⁻¹ cm⁻³

:

9. Activation barrier dependence on electric field

Classical Poole-Frenkel transport between coulombic traps is given by (16-18):

$$J_{\text{PF}} = q \mu N_o E \exp\left(\frac{-q\Phi}{kT}\right) \exp\left[\left(\frac{q^3 E}{\pi \epsilon_o \epsilon}\right)^{1/2} \frac{1}{kT}\right]$$

$$\ln\left[\frac{J}{E}\right] = \ln(q \mu N_o) - \frac{\Phi}{kT} + \left[\frac{q^{3/2}}{(\pi \epsilon_o \epsilon)^{1/2} kT}\right] E^{1/2}$$

where μ is mobility of a detrapped carrier, N_o is the number of traps, E the electric field, Φ is the trap depth, k the Boltzmann constant, and $\epsilon_o \epsilon$ is the dielectric constant. These equations predict that a plot of $\ln(J/E)$ vs $E^{1/2}$ should be linear with a slope that is dependent inversely on temperature. Furthermore, a standard Arrhenius plot of $\ln J$ vs $1/T$ should have a slope of:

$$E_a = -\text{slope of } \ln J \text{ vs } 1/T = -q \Phi/k + \left[\frac{q^{3/2}}{(\pi \epsilon_o \epsilon)^{1/2} k}\right] E^{1/2}$$

Therefore, the slope of a plot of the apparent activation barrier E_a in eV vs $E^{1/2}$ is equal to $(q/\pi \epsilon_o \epsilon)^{1/2}$, which is 0.289 meV cm^{1/2} V^{-1/2} for $\epsilon = 6.9$, as determined from junction capacitance. Figure S8A shows E_a vs $E^{1/2}$ for the indicated thicknesses of BTB in the temperature range 200-300 K. The lines are least-squares fits for the 16 and 22 nm data. The slopes and intercepts are as follows: 16 nm: $y = 0.221x + 350$ ($R^2 = 0.974$); 22 nm: $y = 0.197x + 296$ ($R^2 = 0.967$).

Figure S8B shows Poole-Frenkel plots for a 22 nm BTB junction at four temperatures from 5.8 K to 300 K. According to the equations above, the slopes should vary by a factor of 50 (300/6) in this range, yet in fact vary by only a factor of 1.3.

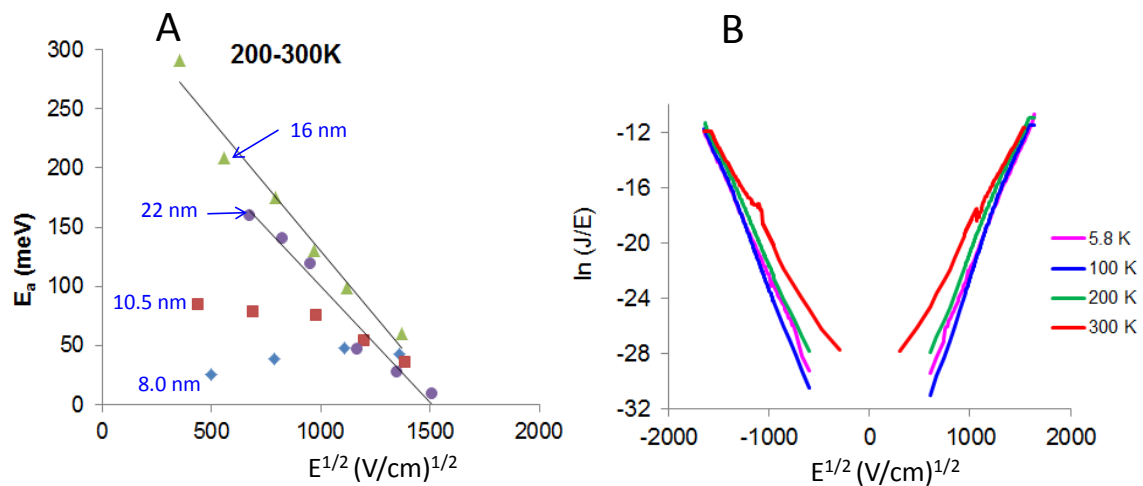


Figure S8. (A) Observed activation energies E_a from Arrhenius plots in the 200-300 K range plotted vs the square root of the electric field. Labels with each set of points indicate the BTB thickness. Lines are least-squares fits to the data for 16 and 22 nm. (B) $\ln(J/E)$ vs $E^{1/2}$ curves for 22 nm BTB junctions at the four temperatures indicated.

References:

1. Bergren AJ, Harris KD, Deng F, & McCreery R (2008) Molecular Electronics using Diazonium-Derived Adlayers on Carbon with Cu Top Contacts: Critical Analysis of Metal Oxides and Filaments. *J. Phys. Condens. Matter* 20:374117.
2. Bergren AJ, McCreery RL, Stoyanov SR, Gusarov S, & Kovalenko A (2010) Electronic Characteristics and Charge Transport Mechanisms for Large Area Aromatic Molecular Junctions. *J. Phys. Chem. C* 114:15806-15815.
3. Bonifas AP & McCreery RL (2010) "Soft" Au, Pt and Cu contacts for molecular junctions through surface-diffusion-mediated deposition. *Nature Nanotechnology* 5(8):612-617.
4. Fave C, *et al.* (2007) Tunable Electrochemical Switches Based on Ultrathin Organic Films. *J. Am. Chem. Soc.* 129(7):1890-1891.
5. Mahmoud AM, Bergren AJ, Pekas N, & McCreery RL (2011) Towards Integrated Molecular Electronic Devices: Characterization of Molecular Layer Integrity During Fabrication Processes. *Adv. Funct. Mater.* 21(12):2273-2281.
6. Sayed SY, Fereiro JA, Yan H, McCreery RL, & Bergren AJ (2012) Charge transport in molecular electronic junctions: Compression of the molecular tunnel barrier in the strong coupling regime. *Proceedings of the National Academy of Sciences* 109(29):11498-11503.
7. Yan H, Bergren AJ, & McCreery RL (2011) All-Carbon Molecular Tunnel Junctions. *J. Am. Chem. Soc.* 133(47):19168-19177.
8. Kumar R, Pillai RG, Pekas N, Wu Y, & McCreery RL (2012) Spatially Resolved Raman Spectroelectrochemistry of Solid-State Polythiophene/Viologen Memory Devices. *J. Am. Chem. Soc.* 134(36):14869-14876.
9. Ru J, Szeto B, Bonifas A, & McCreery RL (2010) Microfabrication and Integration of Diazonium-Based Aromatic Molecular Junctions. *ACS Applied Materials & Interfaces* 2(12):3693-3701.
10. McCreery R, Wu J, & Kalakodimi RJ (2006) Electron Transport and Redox Reactions in Carbon Based Molecular Electronic Junctions. *Phys. Chem. Chem. Physics.* 8:2572-2590.
11. Ranganathan S, McCreery RL, Majji SM, & Madou M (2000) Photoresist-Derived Carbon for Microelectrochemical Applications. *J. Electrochem. Soc.* 147:277 - 282.
12. Kumar R, Yan H, McCreery RL, & Bergren AJ (2011) Electron-beam evaporated silicon as a top contact for molecular electronic device fabrication. *Physical Chemistry Chemical Physics* 13(32):14318-14324.
13. Anariba F, DuVall SH, & McCreery RL (2003) Mono- and Multilayer Formation by Diazonium Reduction on Carbon Surfaces Monitored with Atomic Force Microscopy "Scratching". *Anal. Chem.* 75:3837-3844.
14. Poot M, *et al.* (2006) Temperature Dependence of Three-Terminal Molecular Junctions with Sulfur End-Functionalized Tercyclohexylidenes. *Nano Lett.* 6(5):1031-1035.
15. Eui Yun J, *et al.* (2012) Fibers of reduced graphene oxide nanoribbons. *Nanotechnology* 23:235601.
16. Simmons JG (1967) Poole-Frenkel Effect and Schottky Effect in Metal-Insulator-Metal Systems. *Physical Review* 155(3):657-660.
17. Sze SM (1981) *Physics of Semiconductor Devices* (Wiley, New York) 2nd Edition Ed.
18. Vodenicharov CM & Vodenicharova MB (1980) Schottky and Poole-Frenkel Mechanisms of Conductivity in Thin-Film Me-GeS-Me Systems. *Physica Status Solidi (A)* 57(2):483-487.